



# Detection of early bruises on peaches (*Amygdalus persica* L.) using hyperspectral imaging coupled with improved watershed segmentation algorithm

Jiangbo Li<sup>a,b,c,d</sup>, Liping Chen<sup>a,b,c,d,\*</sup>, Wenqian Huang<sup>a,b,c,d</sup>

<sup>a</sup> Beijing Research Center of Intelligent Equipment for Agriculture, Beijing 100097, China

<sup>b</sup> National Research Center of Intelligent Equipment for Agriculture, Beijing 100097, China

<sup>c</sup> Key Laboratory of Agri-informatics, Ministry of Agriculture, Beijing 100097, China

<sup>d</sup> Beijing Key Laboratory of Intelligent Equipment Technology for Agriculture, Beijing 100097, China

## ARTICLE INFO

### Keywords:

Peach bruise

Hyperspectral imaging

Improved watershed segmentation algorithm

Image processing

## ABSTRACT

Bruise is the most common type of damage to peaches in a major cause of quality loss. However, fast and nondestructive detection of early bruises on peaches is a challenging task. In this study, short-wave near infrared (SW-NIR) and long-wave near infrared (LW-NIR) hyperspectral imaging technologies were observed and compared the ability to discriminate bruised from sound regions. Principal components analysis (PCA) was utilized to select the effective wavelengths for each type of imaging mode. SW-NIR imaging mode was more suitable for detection of early bruises on peaches. A novel improved watershed segmentation algorithm based on morphological gradient reconstruction and marker extraction was developed and applied to the multispectral PC images. The detection results indicated that for all test peaches used in this experiment, 96.5% of the bruised and 97.5% of sound peaches were accurately identified, respectively. A proposed algorithm was superior to the common segmentation methods including Ostu and the global threshold value method. This study demonstrated that SW-NIR hyperspectral imaging coupled with the proposed improved watershed segmentation algorithm could be a potential approach for detection of early bruises on peaches.

## 1. Introduction

Maintaining high-quality fruit is of great importance for the fruit industry in view of ever-increasing consumer awareness of food and agri-products quality and safety (Harker et al., 2003; Zhang et al., 2017a,b). Fruit damage can downgrade fresh fruit quality and even give rise to food safety problems (Nicolai et al., 2014; Fu and Ying, 2014). Bruising is the most common type of fruit damage, which can cause tissue rot due to bacterial and fungal growth and further infect other undamaged fruit during transport and storage, thus resulting in considerable economic loss (Opara and Pathare, 2014). Although commercial sorting systems for fruit damage and defects have been become available, their capability for detecting such subtle defects as bruises is still a problem (Huang et al., 2015). Bruises normally develop below the fruit skin. Damaged tissues need a few hours to become darkened and brownish due to the enzymatic or chemical oxidation of phenolic compounds. Therefore, it is hard to detect bruises on fruit before the visual symptoms occur. Further, even if tissue injury is visible to the naked eye, simple visual inspection that is performed by produce

quality inspectors has problems of subjectivity and inefficiency (Opara and Pathare, 2014). Therefore, fast and nondestructive detection of fruit post-harvest bruises, especially light bruises, is necessary to leave out of wholesome and high- and consistent-quality fruit products.

Advances in computers and electronics have resulted in the development and application of novel automated bruise detection techniques. Different optical detection technologies, such as visible and near infrared spectroscopy (Xing et al., 2006; Luo et al., 2012; Moschetti et al., 2016), X-ray computed tomography (Diels et al., 2017), magnetic resonance imaging (Zion et al., 1995; Milczarek et al., 2009), fluorescence (Chiu and Chen, 2011), thermal imaging (Varith et al., 2003; Baranowski et al., 2012), structured-illumination reflectance imaging (Lu and Lu, 2017), optical coherence tomography images (Zhou et al., 2017), have been applied to study and detect the bruise damage. Visible and near infrared spectroscopy is one of the most often used and efficient tools for the detection of bruises because of its rapidness, inexpensiveness and noninvasive characteristic. However, a major disadvantage of spectroscopic measurement is that it acquires data information from a single and small area on a sample each time, which

\* Corresponding author at: Beijing Research Center of Intelligent Equipment for Agriculture, Beijing 100097, China.  
E-mail address: [chenlp@nercita.org.cn](mailto:chenlp@nercita.org.cn) (L. Chen).

limits its use for surface bruise detection on fruit and may lead to incorrect classification results (Opara and Pathare, 2014). In recent years, hyperspectral imaging as one of the important novel tools has been successfully applied to detect fruit bruises (Xing and Baerdemaeker, 2005; ElMasry et al., 2008; Huang et al., 2015; Keresztes et al., 2016, 2017). Hyperspectral imaging, also known as chemical or spectroscopic imaging, is an emerging technique that integrates conventional imaging and spectroscopy to attain both spatial and spectral information from an object (Gowen et al., 2007; Elmasry et al., 2012). The spectrum of each spatial pixel contains the chemical information of sample substances presented at the corresponding spots on the hyperspectral image. Coupled with appropriate methods, the invisible defective regions can achieve the visual detection based on hyperspectral imaging technique (Li et al., 2016b).

In general, there are two spectral ranges used in the current hyperspectral imaging system, namely visible and short-wave near infrared spectral range (SW-NIR, 400–1000 nm) and long-wave near infrared spectral range (LW-NIR, 1000–1700/2500 nm). Xing and Baerdemaeker (2005) used a hyperspectral imaging system within the wavelength range of 400–1000 nm for bruise detection of 'Jonagold' apples. Principal components analysis (PCA) was used to visualize the hyperspectral data and select the characteristic wavelength images, resulting in a detection rate of 77.8% for the 1-day-old bruises. However, the proposed algorithm was poor for detection of slight bruises. Xing et al. (2005) used the same system coupled with PCA to identify four characteristic wavelength images of 558, 678, 728 and 892. A detection accuracy of 86% was achieved by applying moments thresholding to PCA score image of the four selected images. Xing et al. (2007) combined both chemometric tools and two-thresholding image segmentation algorithm for bruise detection on apples, finding that it was a promising approach. ElMasry et al. (2008) utilized SW-NIR hyperspectral imaging system to detect early bruises on apples. Partial least squares method and stepwise discrimination analysis were used to select three effective wavelength images (750, 820 and 960 nm) in the near infrared region for building the multispectral images. A multilevel adaptive thresholding method was used for segmenting the damaged region of fruit with different timing of bruising. High performance was reached for apples presenting recent (1 h) and old (> 3 days) bruises. Qiang et al. (2011) also used hyperspectral imaging technique to inspect the hidden bruises on kiwifruit. The Vis/NIR (408–1117 nm) hyperspectral image data was collected and multiple optimal wavelength images (682, 723, 744, 810 and 852 nm) were obtained using PCA on the wavelength range from 600 nm to 900 nm. The bruise regions were extracted from the component images of the five waveband images using RBF-SVM classification. The experimental results showed that the error of hidden bruises detection on fruit by means of hyperspectral imaging was 12.5%. Huang et al. (2015) recently developed a multispectral imaging prototype system for real-time detection of bruises. Three effective wavelengths of 780, 850 and 960 nm were selected by a SW-NIR hyperspectral imaging coupled with PCA and the global threshold method were utilized to segment the bruises on apples, resulting in a detection rate of 75% for bruised 'Fuji' apples in an online test with an imaging speed of three apples per second. In addition, some studies on using LW-NIR hyperspectral imaging to detect the bruised fruit were also reported in recent years. Lee et al. (2014) investigated the potential of detecting bruise damages under the pear skin by using hyperspectral imaging with LW-NIR range of 950–1650 nm. A classification algorithm based on *F*-value was applied for analysis of image to find the optimal waveband ratio (R1074/R1016) for the discrimination of bruises and obtained a detection accuracy of 92% for bruises. Keresztes et al. (2016) proposed a real time pixel-based early apple bruise detection system based on hyperspectral technology in the infrared range of 900–2500 nm. Partial least squares-discriminant analysis was used to discriminate bruised pixel spectra from sound pixel spectra. Results showed that system was able to detect fresh bruises (< 2 h) with 98% accuracy at the pixel level with a processing time per

apple below 200 milliseconds. Subsequently, Keresztes et al. (2017) found that spectral area normalization pre-processing was more effective for pixel-based bruise prediction, and post-processing of the binary images by exploiting spatial information further improved the bruise detection accuracy.

These reports indicate that SW-NIR and LW-NIR hyperspectral imaging technologies coupled with appropriate detection algorithm can effectively identify bruised fruit. However, in reality, the detection accuracy is affected by many factors including age of the bruise, type of bruise, bruise severity, type of produce and variety, and pre- and postharvest fruit conditions (Lu, 2003). Therefore, it is difficult to decide which type of system is more suitable for detection of bruises in practice. To our knowledge, to date there has not been reported research on comparing the performance between SW-NIR and LW-NIR hyperspectral imaging for bruise detection of fruit based on the samples under the same conditions. In our study, peaches were selected as they are susceptible to bruising, before and at harvest, and during post harvest operations such as transportation, storage and retail distribution. The specific objectives of this research were to compare the ability between SW-NIR and LW-NIR hyperspectral imaging for early bruise detection of peaches and to select the effective wavelength images for further developing low-cost and real-time multispectral imaging systems in fruit processing plants. And, a novel bruise segmentation algorithm called improved watershed segment algorithm, which is dissimilar from all of the methods mentioned above, was firstly proposed for segmenting the bruised regions on peaches to attain better accuracy of discrimination between bruised and unaffected tissues.

## 2. Materials and methods

### 2.1. Peach samples preparation and bruise treatment

'Pinggu' peach (*Amygdalus persica* L.) is a bicolour cultivar with high variability in the skin color (Li et al., 2016a). Therefore, the early bruise detection of 'Pinggu' peach is very difficult. A total of 200 sound samples with equatorial diameter of approximately 80 mm were purchased from a local fruit supermarket in July 2015. For bruise treatments, bruises were created according to our previous method (Huang et al., 2015). The only difference from our previous method is that bruising was carried out by dropping a steel ball weighing 33 g with a 20 mm diameter onto the peach from a height of 150 mm. Each sample resulted from one to five bruise spots by dropping impact. After the impact, the peaches were stored in the laboratory at 20 °C and 60% RH for 1 h and then hyperspectral images were acquired. From a total of 200 samples, 120 samples were damaged, and the rest were maintained as non-bruised controls. 60 damaged peaches and 40 non-bruised sound peaches were selected randomly from each class as training set to optimize and determine the parameters of detection algorithm, whereas the remaining 100 samples (60 damaged peaches and 40 non-bruised peaches) were used as test set to evaluate the performance of algorithm. Fig. 1(a) showed the RGB image of a sample. The color of bruised region is similar to the color of sound skin around it, thus making it difficult for a human inspector or conventional RGB vision technology to detect it. We expect this work can produce a target image with more obvious contrast between sound and damaged regions to visualize the early bruise, as shown in Fig. 1(b), for accurate detection of bruises on 'Pinggu' peaches.

### 2.2. Hyperspectral image acquisition system

The line-scanning SW-NIR and LW-NIR hyperspectral imaging system as shown in Fig. 2 is composed of two imaging spectrographs (ImSpector V10E and N25E, Spectral Imaging Ltd, Oulu, Finland) attached to a 14-bit SW-NIR thermo-electrically cooled electron multiplying charge-coupled device (EMCCD) camera (Andor Luca EMCCD DL-604 M, Andor Technology plc., N. Ireland) and a 14-bit LW-NIR

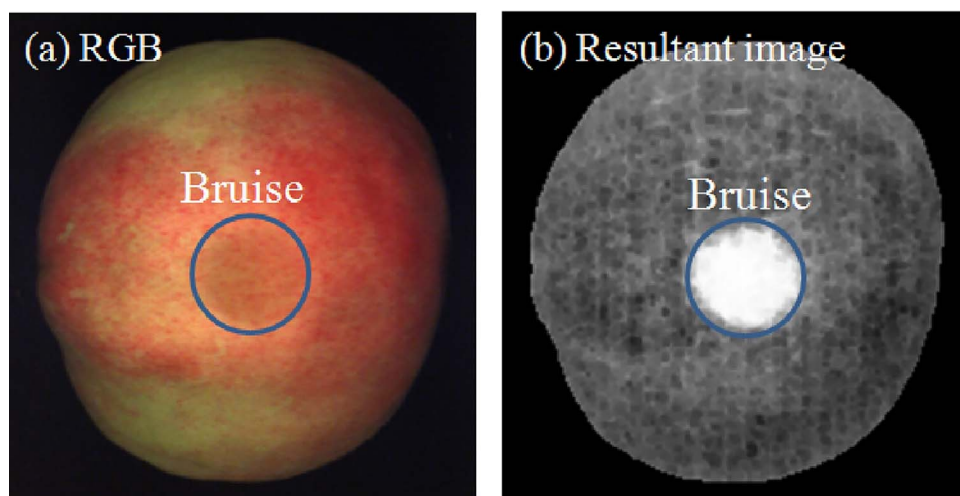


Fig. 1. The images of a bruised sample: (a) RGB image and (b) resultant image after processing.

charge-coupled device camera (Xeva-2.5-320, Xenics Ltd, Belgium), respectively; two 300 W (W) halogen light area sources (Antefore International Co., Ltd., Taiwan, China) with the spectral range of 400–2500 nm providing lighting conditions; a programmable, mobile sample stage (EZHR17EN, AllMotion, Inc., USA) and a computer (Dell OPTIPLEX 990, Intel (R) Core (TM) i5-2400 CPU @ 3.10 GHZ) with spectral image software (Isuzu Optics Corp., Taiwan) and sample stage control software (Isuzu Optics Corp., Taiwan). Two spectrographs in which each has a fixed-size internal slit to define a field of view (FOV) for the spatial line (horizontal pixel direction) and collected spectral images at 0.775 nm intervals within a wavelength range of 325–1100 nm and 6.32 nm intervals within a wavelength range of 930–2548 nm, respectively. The distance from the lens to the sample stage was 400 mm. Two halogen light area sources were mounted at 45° angles from the horizontal, respectively. The hyperspectral imaging system was installed inside an inspection chamber painted with black matte ink to prevent the influence of the external illumination.

To acquire good quality image without saturation and distortion, the movement speed of sample stage and the exposure time of camera were set at 0.8 mm/s, 22 ms and 43 mm/s, 2 ms, respectively, for the SW-NIR and LW-NIR imaging modes. For the experimental run, each peach was manually loaded onto the sample stage and oriented with the side of the fruit that contained the bruises toward the camera. Note that some damaged areas were located on the border rather than the middle of the fruit in the acquired images to simulate a real working environment and develop a more effective algorithm. The camera spectrograph unit was used to scan the peach sample line-by-line as the

sample stage with a stepper motor moved the samples through the FOV of the optical system. Each collected spectral image was stored as a three-dimensional data cube ( $x, y, \lambda$ ) with two spatial dimensions ( $x, y$ ) and one spectral dimension ( $\lambda$ ). The acquired SW-NIR hyperspectral image consists of 1000 congruent sub-images containing intensities at different wavelengths spanned from 325 to 1100 nm and LW-NIR hyperspectral image consists of 256 congruent sub-images containing intensities at different wavelengths spanned from 930 to 2548 nm, respectively. To minimize the effects of noisy signals at opposite ends of the spectrum and the color variation at visible light region, only the spectral range covering 781–1000 nm (282 wavelengths) and 1000–2500 nm (237 wavelengths) were used for the SW-NIR and LW-NIR imaging modes, respectively.

### 2.3. Hyperspectral image calibration

Halogen lamps produce a spatial intensity variation in the plane of the scene and the dark current also exists in the CCD camera, which result in a large amount of noises for some bands with less light intensity. Therefore, the acquired hyperspectral images were first corrected with white and dark references before further data processing and analysis. A white diffuse reflectance board with a 99% reflection efficiency (Spectralon SRT-99-100, Labsphere Inc., North Sutton, NH, USA) was used to obtain a typical white reference image. In addition, because the signal of the camera chip was not zero when no light hit the detectors, thus, a dark current image called dark reference was also acquired to remove the dark current effect of CCD detectors. This dark

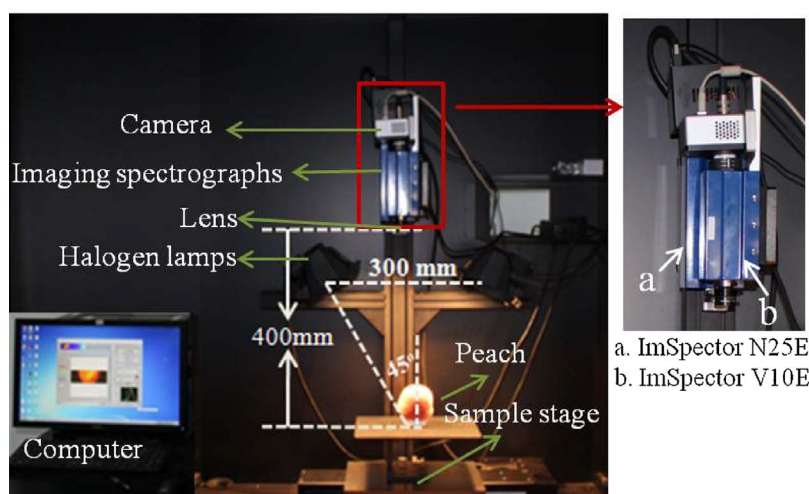


Fig. 2. Hyperspectral imaging system for acquiring SW-NIR and LW-NIR spectral images of 'Pinggu' peaches: (a) imaging spectrograph for LW-NIR hyperspectral imaging and (b) imaging spectrograph for SW-NIR hyperspectral imaging.



current image with 0% reflectance was collected by turning off the lamps and covering the lens with a black cap. The calibrated images  $\rho_{xy}(\lambda)$  was then calculated as follows:

$$\rho_{xy}(\lambda) = \rho_{ref}(\lambda) \frac{R_{xy}(\lambda) - R_{dark}(\lambda)}{R_{white}(\lambda) - R_{dark}(\lambda)} \quad (1)$$

where  $\rho_{ref}(\lambda)$  was the certified reflectance of white reference,  $R_{xy}(\lambda)$  was the acquired original uncorrected hyperspectral image,  $R_{white}(\lambda)$  was the monochrome image acquired by the hyperspectral image system corresponding to the white reference and  $R_{dark}(\lambda)$  was the acquired image corresponding to the dark reference.

## 2.4. Data processing and analysis

### 2.4.1. Principal component analysis (PCA)

Principal component analysis (PCA) has been proved to be an excellent dimensionality reduction method (Xing et al., 2005; Qiang et al., 2011; Huang et al., 2015; Li et al., 2016a,b). Therefore, PCA was used to reduce the spectral dimensionality of hyperspectral reflectance images of peaches, and to aid in determining the effective wavelength images responsible for discriminating bruises from normal peach for each type of hyperspectral imaging mode. In the process of creating the PCA images, a correlation matrix of the image is calculated. This correlation matrix is a diagonal matrix, which is then used to compute the eigenvalues. The eigenvalues are equivalent to the variance of each PC image (Vargas et al., 2005). In this study, PCA on full wavelength images was firstly performed by using ENVI software. Subsequently, all individual PC images were visually evaluated to determine the optimal principal component (PC) image, which could differentiate between bruised and sound tissues. Since each PC image is a linear sum of the original images at individual wavelengths multiplied by the corresponding weighing coefficients (eigenvector), the wavelength images with higher (local maximum) and lower (local minimum) weighting coefficients from the optimal PC image were selected as the effective wavelength images (Vargas et al., 2005; Li et al., 2011, 2016a,b). Finally, the selected images instead of full wavelength images for each imaging mode were re-calculated by PCA to develop the fast multispectral detection algorithm.

### 2.4.2. Improved watershed segmentation method

Based on the re-calculated PC images, effectively segmenting or identifying the bruised region is the most critical step. For performing a fast detection task, some threshold methods, such as the global threshold value and Otsu, have been frequently applied for agricultural product quality detection (Kleynen et al., 2005; Zhao et al., 2010; Ariana and Lu, 2010; Li et al., 2013). The Otsu method is one of the most used approaches to decide the threshold for a satisfied result when the image histogram is bimodal (Otsu, 1979). The global threshold value method was usually used when the objects of interest are well contrasted against the background. However, for bruise detection on peaches, the contrast between bruised and sound regions was different in the obtained multispectral PC images of all the damaged samples. Therefore, it may be difficult to use a global threshold value or Otsu method to segment the bruises on all the peaches. The watershed segmentation as a classical image segmentation algorithm has been widely used for image analysis, especially for the medical and remote sensing fields, because it is rapid, simple and intuitive (Ng et al., 2006; Chevretil et al., 2007; Mustaqeem et al., 2012; Li et al., 2010). However, drawbacks such problems as over-segmentation and sensitivity to false edges can be observed (Grau et al., 2004). In this paper, an improved watershed segmentation algorithm based on morphological gradient reconstruction and marker extraction was proposed to segment the damaged region. The proposed algorithm includes three successive steps, namely morphological gradient enhancement, morphological reconstruction and marker-controlled watershed segmentation.

**2.4.2.1. Morphological gradient enhancement.** Compared with original multispectral PC images, gradient transformation can more effectively reflect the changes among regions on the peach surface, and further enhance the changes of gray-scale from the different regions in the input image. Therefore, the image was usually preprocessed by gradient amplitude transformation before performing the watershed segmentation. The gradient amplitude image can be obtained by applying different differential operators such as ‘Sobel’ and ‘Prewitt’ to original image. However, these differential operators were sensitive to noises on the peach surface, therefore, the gradient image was obtained by morphological gradient method in this study. The morphological gradient of image  $f(x,y)$  was defined as follows:

$$\nabla[f(x,y)] = (f \oplus b)(x,y) - (f \ominus b)(x,y) \quad (2)$$

where  $f(x,y)$  and  $b(x,y)$  are the processed image and structuring element, respectively, whereas symbols about ‘ $\oplus$ ’ and ‘ $\ominus$ ’ represent morphological dilation and erosion operations, respectively. In terms of structuring element, the morphological gradient relies less on edge direction if symmetric structuring element is used. Thus, the ‘disk’ structuring element, which is isotropic and can effectively eliminate the dependence of the gradient on edge direction, is used.

**2.4.2.2. Morphological reconstruction.** After using the morphological gradient enhancement processing, edge information of different regions on the peach was enhanced. However, some noises and details in the morphological gradient image were also enhanced and sharpened. The over-segmentation phenomena cannot be avoided if conventional watershed segmentation algorithm is directly used. Therefore, a morphological ‘opening and closing’ operation was employed to perform morphological image reconstruction based on gradient image  $\nabla[f(x,y)]$  before standard watershed segmentation was used. Reconstruction operation can remove the local extremes caused by close texture and noise, furthermore, the outline of different regions on the peach was recovered during morphological reconstruction to retain the main information in the object shape while simplifying the image. Morphological ‘opening and closing’ reconstruction operation is based on the geodesic dilation and erosion (Salembier and Pardas, 1994). For gradient image  $\nabla[f(x,y)]$ , reference image  $r(x,y)$  and structuring element  $b(x,y)$ , the morphological geodesic dilation was defined as follows:

$$\begin{cases} D_b^1(\nabla f(x,y), r) = \min(\nabla f(x,y) \oplus b, r) \\ D_b^{i+1}(\nabla f(x,y), r) = \min(D_b^i \oplus b, r) (i = 1, 2, 3, \dots) \end{cases} \quad (3)$$

Geodesic dilation is defined by iterations. When the iteration number is equal to preset value or  $D_b^{i+1}(\nabla f(x,y), r) = D_b^i(\nabla f(x,y), r)$ , the iteration is over. Here, we thought that the iteration was over when both values were equal. On the basis of above definition, morphological opening reconstruction  $O_b^{(rec)}$  was defined as follows:

$$O_b^{(rec)}[\nabla f(x,y), r] = D_b^{(rec)}[\nabla f(x,y) \ominus b, r] \quad (4)$$

Similarly, the morphological geodesic erosion was defined as follows:

$$\begin{cases} E_b^1(\nabla f(x,y), r) = \max(\nabla f(x,y) \ominus b, r) \\ E_b^{i+1}(\nabla f(x,y), r) = \max(E_b^i \ominus b, r) (i = 1, 2, 3, \dots) \end{cases} \quad (5)$$

On the basis of erosion operation, morphological closing reconstruction  $C_b^{(rec)}$  was defined as follows:

$$C_b^{(rec)}[\nabla f(x,y), r] = E_b^{(rec)}[\nabla f(x,y) \oplus b, r] \quad (6)$$

where symbols about ‘ $\circ$ ’ and ‘ $\bullet$ ’ stand for morphological opening and closing operations, respectively. Finally, a morphological ‘opening and closing’ operation  $OC_b^{(rec)}$  was defined as follows:

$$OC_b^{(rec)}[\nabla f(x,y), r] = C_b^{(rec)}[O_b^{(rec)}(\nabla f(x,y), r), r] \quad (7)$$

**2.4.2.3. Marker-controlled watershed segmentation.** Although most of the regional extremes and noises were eliminated after the morphological ‘opening and closing operation’ reconstruction, some minimum target points that had nothing to do with the objects of interest remained. Therefore, the objects of interest were divided into numerous meaningless small areas. If the objects of interest can be obtained before watershed segmentation transformation, these objects can be used to suppress the meaningless minimum target points, thus avoiding the over-segmentation phenomena. Here, the threshold value method was used for marker extraction from the image after morphological reconstruction to obtain the target points belonged to the damaged regions. Firstly, all local minimum regions were detected in the gradient image. Then, each local minimum region was judged if it is bigger than a set threshold, and the minimum region that was larger than the threshold was marked. After the foregoing process, a binary image that marked the local minimum region based on the threshold value  $t$  was obtained by following formula:

$$g_t(x, y) = \begin{cases} 1 & OC_b^{(rec)}(x, y) > t \\ 0 & \text{otherwise} \end{cases} \quad (8)$$

The gradient image was then modified by the minimum regions (called markers) retained in the  $g_t(x, y)$ . Finally, the watershed transformation was applied to the modified gradient image. To further evaluate the performance of the proposed improved watershed segmentation method (I-WSM), as comparison, the global threshold value method, Otsu and conventional watershed segmentation method (C-WSM) were utilized to segment the bruises on the peaches.

Environment for Visualizing Images Software Program (ENVI 4.6, Research System Inc., Boulder, CO., USA) and MATLAB R2008b software (The Math Work, Inc., Natick, MA, USA) were used to process and analyze all the hyperspectral images.

### 3. Results and discussion

#### 3.1. Overview of spectra and images

Representative spectra extracted from regions of interest (ROIs) in the SW-NIR and LW-NIR hyperspectral images of peaches are shown in Fig. 3a and b, respectively. In this study, the ROI was manually selected in a scroll window using the rectangle drawing mode provided by ENVI ROI tools (ENVI 4.6, Research System Inc., Boulder, CO., USA). Each ROI contains approximately 2000 pixels for calculating the mean spectra. To decrease spectral variability due to peach curvature, spectra of two ROIs including bruise region and sound region were extracted from the middle of samples for each type of hyperspectral images. These ROIs were selected from the similar center area, although the specular reflection phenomenon was existing in the center portion of

samples. As seen in Fig. 3a and b, two spectral curves from each type imaging mode showed similar shape features. And, the intensities of spectra of sound regions were higher than those of bruise regions in the whole SW-NIR or LW-NIR wavelength ranges, respectively. As a matter of fact, these characteristics were also observed in other areas on samples without the specular reflection phenomena. Similar results have been observed (ElMasry et al., 2008; Lee et al., 2014; Huang et al., 2015). Based on these characteristics, it seems to imply that only a single-band image was enough for each imaging mode to identify the bruises. To verify this viewpoint, single-band images at 970 nm for SW-NIR and 1065 nm for LW-NIR hyperspectral images were selected and the intensity distribution of images were visualized by pseudo-color image processing. The pseudo-color images of both single-band images were also shown in Fig. 3a and b, respectively. In these two pictures, different colors correspond to different gray levels. The gray level gradually increases from mazarine blue to dark red. Obviously, it can be found from pseudo-color images that bruise region has the higher intensity values than those of the sound region near the edge of fruit by a visual assessment. Therefore, the spectra shown in Fig. 3a and b do not account for the spatial variations in the intensities from the center portions toward the edges. Thus, it was impossible to segment the damaged region by a single-band image in the SW-NIR or LW-NIR spectral ranges because of the non-uniform light intensity distribution on the spherical peach surface, which was in agreement with results achieved from our previous work on oranges and peaches (Li et al., 2011, 2016a,b).

#### 3.2. PCA in the SW-NIR and LW-NIR wavelength ranges

The first five PC images (denoted by PC1 to PC5) obtained from the PCA of the hyperspectral reflectance images of a typical bruise sample based on the SW-NIR (781–1000 nm) and LW-NIR (1000–2500 nm) wavelength ranges are shown in Fig. 4a and b, respectively. The first row of each figure, respectively, stands for the real PC image. To obtain a more clear comparison, the pseudo-color images corresponding to different PC images are also shown in the second row of each figure, respectively. In general, the PC1 image that represents the average grey value information of the fruit surface over the full spectral region does not provide more unique features than the original, untransformed hyperspectral images. As can be seen, the bruised region was more obvious in PC2, PC3 and PC4 images and PC images starting from PC5 were no longer useful information for two types of imaging modes, respectively. Based on further visual assessment for PC2, PC3 and PC4 images shown in Fig. 4a, it was noted that PC4 with more uniform intensity distribution can offer the best contrast between sound tissue and damaged tissue. On the contrary, PC2 and PC3 images were more sensitive to peel color and peach surface curvature. Similar phenomena

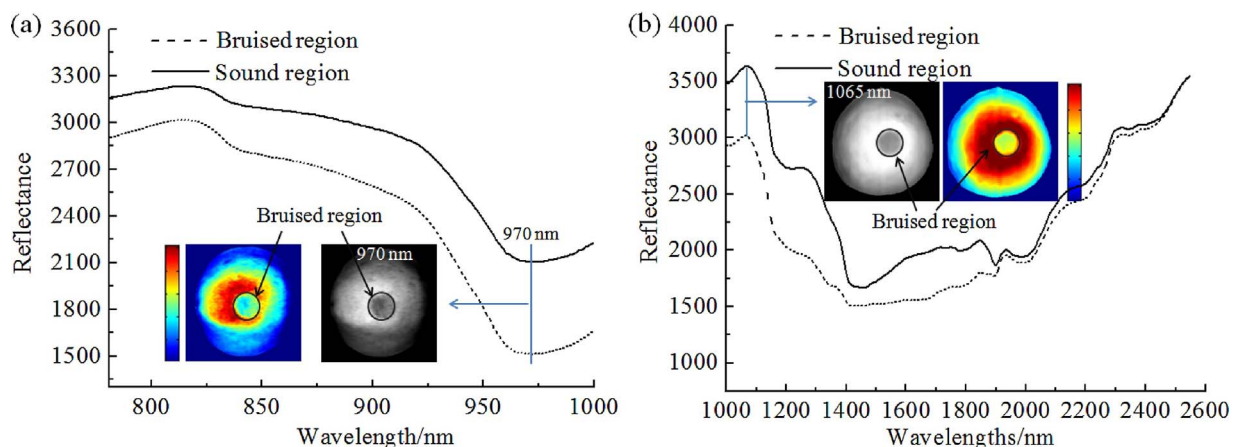


Fig. 3. Representative reflectance spectra of ROIs and single-band images for SW-NIR and LW-NIR wavelength regions, respectively.

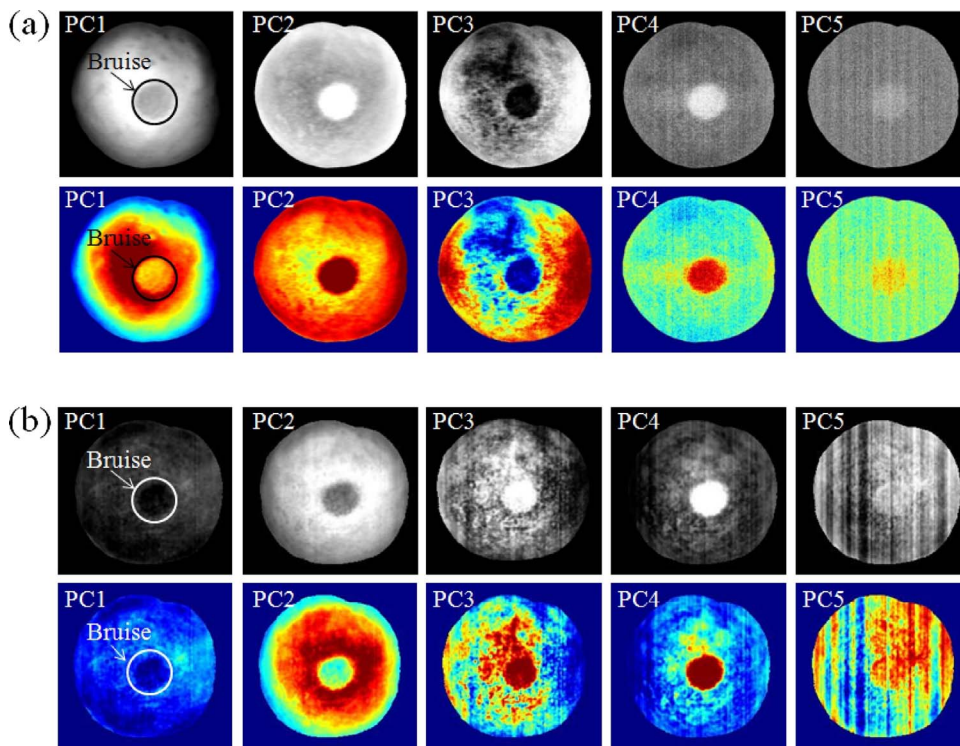


Fig. 4. The first five PC images (PC1–PC5) obtained using (a) SW-NIR full-wavelength region from 781 to 1000 nm and (b) LW-NIR full-wavelength region from 1000 to 2500 nm for bruise detection of peaches, respectively.

can be also found in Fig. 4b. Therefore, PC4 images were chosen for bruise detection on the peaches. However, it has a problem of using too many spectral channels (282 wavelengths for SW-NIR mode and 237 wavelengths for LW-NIR mode) for PCA, making it impossible to develop a fast multispectral system for detection of bruises. Thus, effective wavelengths were selected by analyzing the weighing coefficients of PC4 obtained from each type of imaging mode, respectively.

### 3.3. Selection of effective wavelength images

The weighing coefficient curves of PC4 obtained from each type of imaging mode based on full wavelength ranges of 781–1000 nm and 1000–2500 nm are shown in Fig. 5a and b, respectively. The peaks and valleys in the curves indicated the effective wavelengths that made great contributions to the corresponding PC4 images (Vargas et al., 2005). Therefore, five wavelengths from SW-NIR region and six wavelengths from LW-NIR region can be chosen as effective wavelengths, which were centered at around 781, 816, 840, 945, 1000 nm and 1000, 1065, 1260, 1460, 1917, 2500 nm for two kinds of imaging modes, respectively. The obtained five effective wavelengths from SW-NIR

region were mainly related to the second and third overtones of oxygen-hydrogen (O–H) stretches, and third and fourth overtones of carbon-hydrogen (C–H) stretches of the organic molecules. And, six effective wavelengths from LW-NIR region was associated with the second overtone of band C–H, the stretching first overtone of bond O–H in H<sub>2</sub>O and the combination tone of water. These effective wavelengths include some dominant water absorption peaks and other no water absorption peaks, indicating that the differences between bruised tissue and sound tissue might not only have a relationship with change of water content, but also change of other organic molecules such as fructose, glucose and pectin in peaches.

### 3.4. PCA on the selected effective wavelengths

After obtaining the effective wavelengths for each type of imaging mode, PCA was performed again based on the corresponding wavelength images. The resultant multispectral PC images for SW-NIR and LW-NIR types are shown in Fig. 6a and b, respectively. For a clear observation, the pseudo-color images corresponding to different PC images are shown in the second row of each figure. As can be seen, the

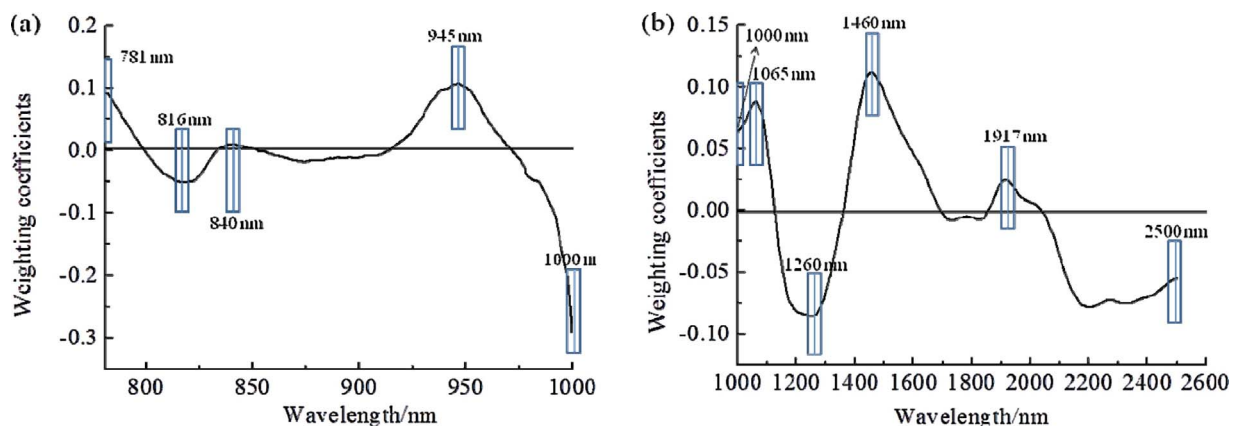


Fig. 5. Weighing coefficient curves of PC4 images obtained from full-wavelength PCA based on SW-NIR and LW-NIR wavelength ranges, respectively.



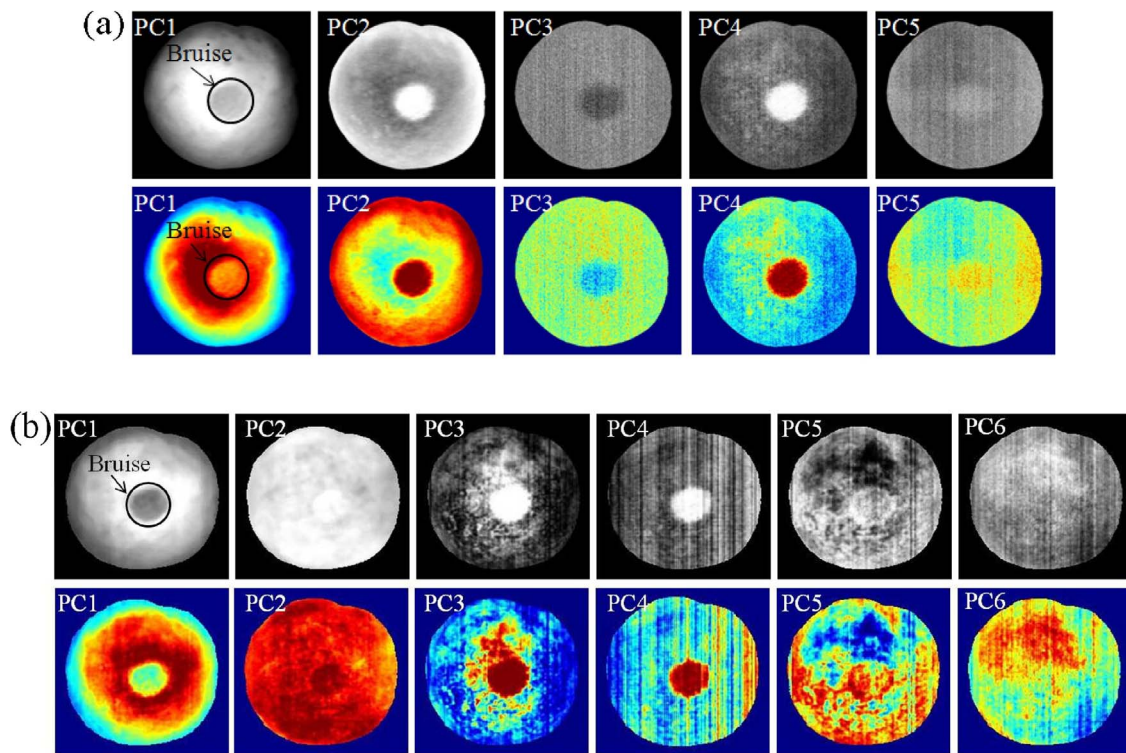


Fig. 6. PC images obtained using the selected effective wavelengths in the (a) SW-NIR and (b) LW-NIR spectral regions for bruise detection of peaches.

multispectral PC4 images obtained the best results for SW-NIR or LW-NIR hyperspectral imaging systems, respectively. Compared with full wavelength PC4 images shown in Fig. 4a and b, the multispectral PC4 images of each type of imaging mode has a similar or slightly better result. Moreover, the multispectral PC4 image obtained from SW-NIR was superior to LW-NIR because of more clear contrast between bruised and sound regions by comparing both Fig. 6a and b. PC4 image obtained from LW-NIR contains some obvious noises, especially on the edge region of fruit image, which can easily lead to misjudgment and further decrease the detection accuracy for sound samples. All samples in the training set were analysis and the similar visual results can be observed. Thus, PC4 images from SW-NIR hyperspectral imaging mode as object images were used for subsequent bruise detection.

### 3.5. Bruises segmentation

Although the effective multispectral PC images were obtained by PCA twice, successfully segmenting bruised regions on the PC4 image is a challenging task because not all samples that were similar to peach in the example have the clear contrast between bruised spots and sound regions. Therefore, development of effective segmentation algorithm is one of main aims of this study. Performance of the proposed improved watershed segmentation method (I-WSM) based on morphological gradient reconstruction and marker extraction was compared with the global threshold value method, Otsu and conventional watershed segmentation method (C-WSM) for bruise detection of peaches. All samples mainly include four classes, namely class I, class II, class III and class IV. For these four classes, an example of bruise segmentation by using the different algorithms is shown in Fig. 7. The illustrated eleven samples were selected from training set. In Fig. 7, class I has two damaged samples and the bruised spots were on the middle region and edge region, respectively. Class II represents those samples with multiple bruised spots. Class III stands for the samples with concave line and concave line appears in different position in the image. Class IV is the sound fruit type including a sample with stem, a sample with calyx and a sample without stem and calyx. As can be seen, for all sample types,

bruised regions are randomly distributed on the peaches for simulating the real working conditions. In Fig. 7, pictures from the first to the fourth rows stand for original RGB images, multispectral PC4 images, pseudo-color images, I-WSM results from PC4 image and pictures from the last four rows stand for binary resultant images after applying I-WSM, Otsu, the global threshold value method and C-WSM, respectively. The circle marks on the RGB images are the location of damaged regions. Compared among the resultant images from the fourth row to last row, the proposed I-WSM can exactly segment the bruises as shown in the fourth and fifth rows of images, showing the robust detection performance. On the contrary, C-WSM generated the worst bruises segmentation results due to the over-segmentation with numerous meaningless small areas, as shown in the last row of Fig. 7. In this study, the Otsu and global threshold value method were also used for segmentation of bruises considering the universality of threshold methods. The segmented results of bruises were shown in the sixth and seventh rows of Fig. 7. The Otsu method can obtain a satisfied result when the image histogram is bimodal, but its ability will reduce when there is the obvious transitional region between two peaks. As shown in the sixth row of Fig. 7, although all bruised regions on these samples were detected, the incorrect segmentation with false positive was apparent on some samples because of existence of the transitional region. The transitional region can be seen in the histogram (shown in Fig. 8) of the second image of class III for an example. Compared with Otsu method, the global threshold value method with 190 of threshold (T) obtained the better detection results. It should be noted, however, that not all bruised spots on the peaches have the same contrast in the obtained multispectral PC images. For instance, the bruised spot on the right of the third image of class II has the similar gray level to some sound regions on the second image of class III. Thus, a lot of sound tissues with higher gray level will be misclassified if those damaged regions with lower gray level need be successfully segmented based on the PC4 images, which may be a chief problem for use of the global threshold value method. In other words, the global threshold value method is unreliable. In addition, it could be also observed from PC images of class III and class IV that the characteristic concave line and calyx on

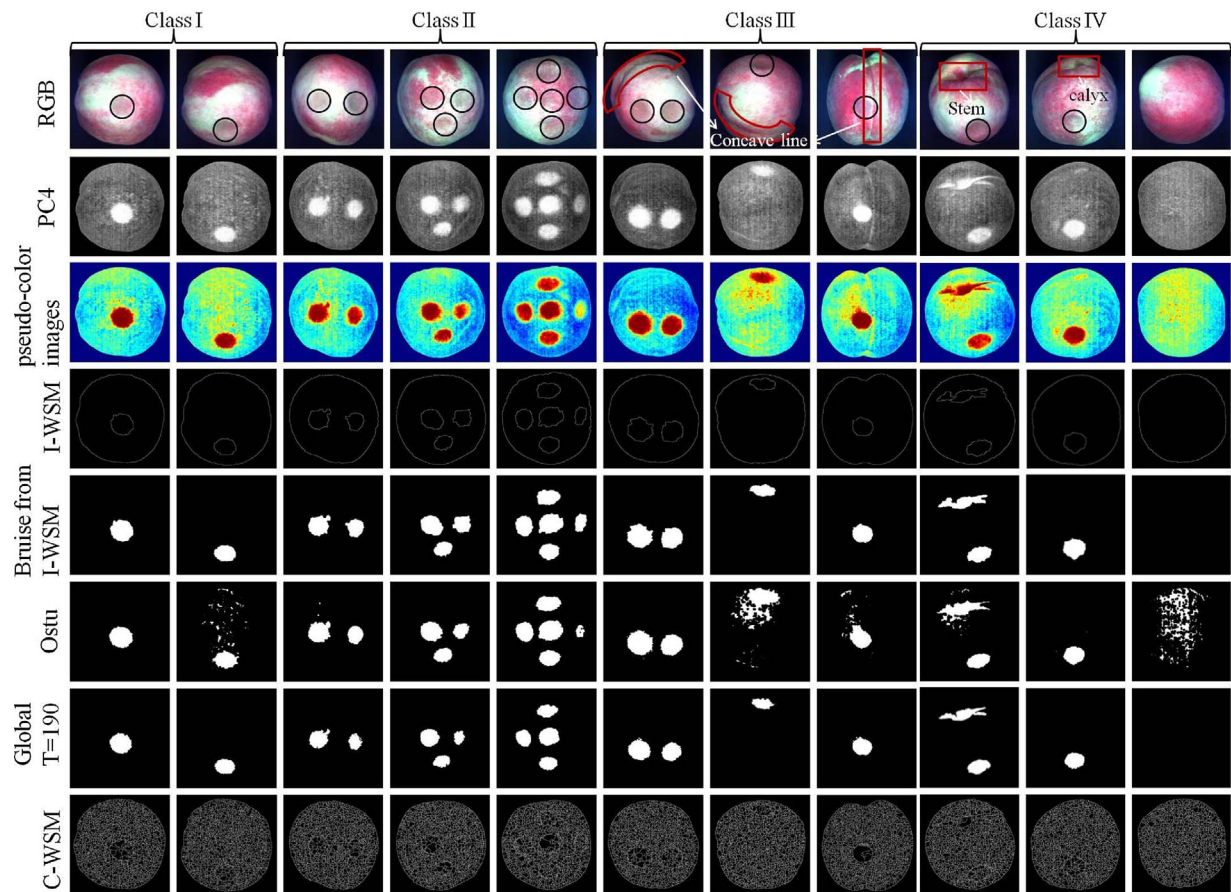


Fig. 7. Example of bruise segmentation by using the different algorithms. Original RGB images (first row), multispectral PC4 images (second row), pseudo-color images (third row), I-WSM results from PC4 image (fourth row), bruised regions after I-WSM (fifth row), Otsu (sixth row), Global threshold value method (seventh row) and C-WSM (eighth row), respectively.

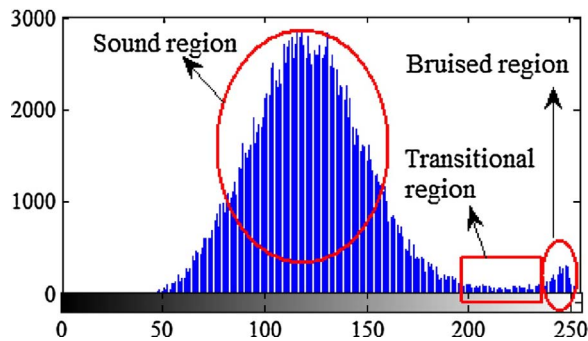


Fig. 8. The histogram of the second image of class III.

the peaches has a similar intensity to sound region, while stem was easily misidentified as damaged region based on only intensity information. Thus, a new discrimination factor, namely the circularity ( $R$ ), was added in the detection algorithm. To be more specific, the nonzero regions in the resultant binary image obtained by I-WSM, the global threshold value method or Otsu were firstly labeled. Then, the circularity ( $R$ ) of every labeled region was respectively calculated as follows:

$$R = 4\pi A/P^2 \quad (9)$$

where  $A$  and  $P$  are the area and perimeter of each labeled region, respectively. If  $R \geq 0.65$ , the labeled region stands for a damaged region and the algorithm subsequently judged this fruit to be a bruised peach. And, if  $R < 0.65$ , the labeled region was thought as stem and this region will be changed into zero showing the sound region in the resultant binary image. Based on this discrimination factor and strategy,

**Table 1**  
Detection results of the bruised regions on the all damaged samples from the training set and test set by using different segmentation algorithms.

Methods	Training set (sample number = 60)			Test set (sample number = 60)		
	No. of actual bruise regions	No. of detected bruise regions	Accuracy (%)	No. of actual bruise regions	No. of detected bruise regions	Accuracy (%)
T = 190	100	90	90%	113	103	91.2%
Otsu	100	98	98%	113	110	97.3%
I-WSM	100	97	97%	113	109	96.5%



**Table 2**

Detection results for all the sound samples in the training set and test set by using different segmentation algorithms.

Methods	Training set (sample number = 40)			Test set (sample number = 40)		
	No. of sound peaches	Misclassified	Accuracy (%)	No. of sound peaches	Misclassified	Accuracy (%)
T = 190	40	2	95%	40	2	95%
Ostu	40	17	57.5%	40	20	50%
I-WSM	40	0	100%	40	1	97.5%

the stem region in the first image of class IV can be accurately identified and removed in the resultant binary images. In this case, the circularities of stem region and bruised region are 0.30 and 0.85, respectively.

In this study, I-WSM algorithm has three important parameters, respectively, the structuring elements of morphological gradient enhancement and reconstruction and the height threshold of mark. The ‘disk’ structuring elements with  $2 \times 2$  kernel size and  $8 \times 8$  kernel size and height threshold 35 were selected for the three parameters, respectively. The threshold (T) used in the global threshold value method was equal to 190. In terms of image preprocessing, morphological filtering was used with an aim to remove undesired small size pixels (noises) in the resultant binary images during the development of whole algorithm. All parameters were obtained by statistical analysis from all training samples. In the actual application, these parameters can be conveniently adjusted based on practical working conditions.

### 3.6. Defect detection results

The proposed multispectral algorithms for fast detection of early bruises on the ‘Pinggu’ peaches were evaluated using all samples including 120 damaged peaches and 80 sound peaches. To more accurately evaluate the ability of algorithms, each bruised spot on the samples was recorded. Thus, 100 and 113 bruised spots were marked in the training set and test set, respectively. For all bruised regions, the detection results based on three segmentation methods were shown in Table 1. Note that the result from C-WSM was not listed because this method cannot effectively segment the bruises, as shown in Fig. 7. Table 2 shows that detection results for all the sound samples in the training set and test set by using different segmentation algorithms. As shown in Table 1, the Ostu method obtained the best bruise segmentation results with 98% and 97.3% detection accuracies for training set and test set, respectively. Although the Ostu method has the good performance for detection of bruised regions, it also has the worst ability for detection of sound samples with 57.5% and 50% detection accuracies for training set and test set as shown in Table 2, respectively. Compared with the Ostu method, both the I-WSM and the global threshold value method have the more balanced abilities for detection of bruised and sound samples. Based on these two methods, detection accuracies of bruised regions and sound samples from test sets achieved 96.5%, 97.5% and 91.2%, 95%, respectively, as shown in Tables 1 and 2. Therefore, it was very obvious that I-WSM couple with multispectral PC image obtained the best detection results for early bruises by comprehensively considering all samples. For the proposed I-WSM, the misjudgment often occurs under three cases. These three cases were also shown in Table 1. Case 1 might happen when the damaged region located on the extreme edge of the image because less and weaker light can be only received by camera CCD. However, it does not imply losing efficacy, since multiple images of each sample were usually collected by way of fruit rotation in the online automatic fruit inspection (Zhang et al., 2017a,b), thus allowing the detection system to inspect most of the fruit surface by acquiring different images while fruit pass below the camera. For case 2, it is bound to happen when the ridge line of bruised region and edge line of peach was linked to form a connected region. Like case 1, this case can be also avoided in practice due to rotation detection of fruit. However, for the third case, the bruised region on the right of PC image has the unobvious contrast with sound

region might due to very slight damage, which cannot be avoided by using the recent segmentation algorithm. Some image enhancement methods may be necessary for solving this problem.

## 4. Conclusions

This study observed and compared the ability between SW-NIR and LW-NIR hyperspectral imaging for early bruise detection of ‘Pinggu’ peaches. SW-NIR technology was more effective due to very obvious contrast between damaged region and sound region on the PC images. With the use of PCA, five effective wavelength images centered at around 781, 816, 840, 945, 1000 nm were selected. The wavelength images explored in this study could be helpful for developing low-cost and real-time multispectral systems for detecting bruises on peaches. An improved watershed segment algorithm that was superior to Ostu and the global threshold value methods were developed to segment the bruises from sound tissues based on multispectral PC4 scores images, and the satisfactory classification results with bruise detection accuracy of 96.5% and sound sample detection accuracy of 97.5% for test set were obtained. This study lays a foundation for later development of a computer vision system for bruise detection. The proposed navel segmentation algorithm could also provide a useful reference for detection of other type of peel defects on fruit. Further studies will focus on establishing a more efficient multi-spectral imaging system and improving the detection accuracy of bruised fruit coupled with image enhancement method, and also further optimizing the proposed watershed segmentation algorithm with larger sample numbers and more cultivars.

## Acknowledgements

The authors gratefully acknowledge the financial support provided by the National Key Technologies R&D Program (Project No. 2015BAD19B03), the Young Scientist Fund of Beijing Academy of Agriculture and Forestry Sciences of China (Project No. QNJJ201528), Beijing Nova program (No. Z171100001117035) and the Science and Technology Innovation Ability Construction Project of Beijing Academy of Agriculture and Forestry Science (Project No. KJCX20170417).

## References

- Ariana, D.P., Lu, R., 2010. Evaluation of internal defect and surface color of whole pickles using hyperspectral imaging. *J. Food Eng.* 96, 583–590.
- Baranowski, P., Mazurek, W., Wozniak, J., Majewska, U., 2012. Detection of early bruises in apples using hyperspectral data and thermal imaging. *J. Food Eng.* 110, 345–355.
- Chevrefils, C., Chérier, F., Grimard, G., Aubin, C.E., 2007. Watershed segmentation of intervertebral disk and spinal canal from MRI images. *Int. Conf. Image Anal. Recognit.* 4633, 1017–1027.
- Chiu, Y.C., Chen, M.T., 2011. A study of apple bruise detection by using chlorophyll fluorescence image. In: 2011 ASABE Annual International Meeting Sponsored by ASABE. Gault House Louisville, Kentucky, August 7–10, 2011.
- Diels, E., Dael, M., Keresztes, J., Vanmaercke, S., Verboven, P., Nicolai, B., Saeys, W., Ramon, H., Smeets, B., 2017. Assessment of bruise volumes in apples using X-ray computed tomography. *Postharvest Biol. Technol.* 128, 24–32.
- ElMasry, G., Wang, N., Vigneault, C., Qiao, J., ElSayed, A., 2008. Early detection of apple bruises on different background colors using hyperspectral imaging. *LWT- Food Sci. Technol.* 41, 337–345.
- Elmasry, G., Kamruzzaman, M., Sun, D.W., Allen, P., 2012. Principles and applications of hyperspectral imaging in quality evaluation of agro-food products: a review. *Crit. Rev. Food Sci. Nutr.* 52 (11), 999–1023.

- Fu, X.P., Ying, Y.B., 2014. Food safety evaluation based on near infrared spectroscopy and imaging: a review. *Crit. Rev. Food Sci. Nutr.* <http://dx.doi.org/10.1080/10408398.2013.807418>.
- Gowen, A.A., O'Donnell, C.P., Cullen, P.J., Downey, G., Frias, J.M., 2007. Hyperspectral imaging—an emerging process analytical tool for food quality and safety control. *Trends Food Sci. Technol.* 18, 590–598.
- Grau, V., Mewes, A.U.J., Alcaniz, M., Kikinis, R., Warfield, S.K., 2004. Improved watershed transform for medical image segmentation using prior information. *IEEE Trans. Med. Imaging* 23 (4), 447–458.
- Harker, F.R., Gunson, F.A., Jaeger, S.R., 2003. The case for fruit quality: an interpretive review of consumer attitudes, and preferences for apples. *Postharvest Biol. Technol.* 28 (3), 333–347.
- Huang, W.Q., Li, J.B., Wang, Q.Y., Chen, L.P., 2015. Development of a multispectral imaging system for online detection of bruises on apples. *J. Food Eng.* 145, 62–71.
- Keresztes, J.C., Goodarzi, M., Saeys, W., 2016. Real-time pixel based early apple bruise detection using short wave infrared hyperspectral imaging in combination with calibration and glare correction techniques. *Food Control* 66, 215–226.
- Keresztes, J.C., Diels, E., Goodarzi, M., Nguyen-Do-Trong, N., Goos, P., Nicolai, B., Saeys, W., 2017. Glare based apple sorting and iterative algorithm for bruise region detection using shortwave infrared hyperspectral imaging. *Postharvest Biol. Technol.* 130, 103–115.
- Kleynen, O., Leemans, V., Destain, M.F., 2005. Development of a multi-spectral vision system for the detection of defects on apples. *J. Food Eng.* 69, 41–49.
- Lee, W.H., Kim, M.S., Lee, H., Delwiche, S.R., Bae, H., Kim, D.Y., Cho, B.K., 2014. Hyperspectral near-infrared imaging for the detection of physical damages of pear. *J. Food Eng.* 130, 1–7.
- Li, D., Zhang, G., Wu, Z., Yi, L., 2010. An edge embedded marker-based watershed algorithm for high spatial resolution remote sensing image segmentation. *IEEE Trans. Image Process.* 19 (10), 2781–2787.
- Li, J.B., Rao, X.Q., Ying, Y.B., 2011. Detection of common defects on oranges using hyperspectral reflectance imaging. *Comput. Electron. Agric.* 78 (1), 38–48.
- Li, J.B., Rao, X.Q., Wang, F.J., Wu, W., Ying, Y.B., 2013. Automatic detection of common surface defects on oranges using combined lighting transform and image ratio methods. *Postharvest Biol. Technol.* 82, 59–69.
- Li, J.B., Chen, L.P., Huang, W.Q., Wang, Q.Y., Zhang, B.H., Tian, X., Fan, S.X., Li, B., 2016a. Multispectral detection of skin defects of bi-colored peaches based on vis-NIR hyperspectral imaging. *Postharvest Biol. Technol.* 112, 121–133.
- Li, J.B., Huang, W.J., Tian, X., Wang, C.P., Fan, S.X., Zhao, C.J., 2016b. Fast detection and visualization of early decay in citrus using Vis-NIR hyperspectral imaging. *Comput. Electron. Agric.* 127, 582–592.
- Lu, Y.Z., Lu, R.F., 2017. Using composite sinusoidal patterns in structured-illumination reflectance imaging (SIRI) for enhanced detection of apple bruise. *J. Food Eng.* 199, 54–64.
- Lu, R., 2003. Detection of bruises on apples using near-infrared hyperspectral imaging. *Trans. ASAE* 46 (2), 523–530.
- Luo, X., Takahashi, T., Kyo, K., Zhang, S., 2012. Wavelength selection in vis/NIR spectra for detection of bruises on apples by ROC analysis. *J. Food Eng.* 109, 457–466.
- Milczarek, R.R., Saltveit, M.E., Garvey, T.C., McCarthy, M.J., 2009. Assessment of tomato pericarp mechanical damage using multivariate analysis of magnetic resonance images. *Postharvest Biol. Technol.* 52, 189–195.
- Moscetti, R., Haff, R.P., Monarca, D., Cecchini, M., Massantini, R., 2016. Near-infrared spectroscopy for detection of hailstorm damage on olive fruit. *Postharvest Biol. Technol.* 120, 204–212.
- Mustaqeem, A., Javed, A., Fatima, T., 2012. An efficient brain tumor detection algorithm using watershed & thresholding based segmentation. *Int. J. Image Graphics Signal Process.* 10, 34–39.
- Ng, H.P., Ong, S.H., Foong, K.W.C., Goh, P.S., Nowinski, W.L., 2006. Medical image segmentation using k-means clustering and improved watershed algorithm. *IEEE Southwest Symp. Image Anal. Interpretation* 2006, 61–65.
- Nicolai, B.M., Defraeye, T., Ketelaere, B.D., Herremans, E., Hertog, M.L.A.T.M., Saeys, W., Torricelli, A., Vandendriessche, T., Verboven, P., 2014. Nondestructive measurement of fruit and vegetable quality. *Annu. Rev. Food Sci. Technol.* 5, 285–312.
- Opara, U.L., Pathare, P.B., 2014. Bruise damage measurement and analysis of fresh horticultural produce: a review. *Postharvest Biol. Technol.* 91, 9–24.
- Otsu, N., 1979. Threshold selection method from gray-level histograms. *IEEE Trans. Syst. Man Cybern.* 9 (1), 62–66.
- Qiang, L., Tang, M.J., Cai, J.R., Zhao, J.W., Vittayapadung, S., 2011. Vis/NIR hyperspectral imaging for detection of hidden bruises on kiwifruits. *Czech J. Food Sci.* 29 (6), 595–602.
- Salembier, P., Pardas, M., 1994. Hierarchical morphological segmentation for image sequence coding. *IEEE Trans. Image Process.* 3 (5), 639–651.
- Vargas, A.M., Kim, M.S., Tao, Y., Lefcourt, A.M., Chen, Y.R., Luo, Y., Song, Y., Buchanan, R., 2005. Defection of fecal contamination on cantaloupes using hyperspectral fluorescence imagery. *J. Food Sci.* 70 (8), 471–476.
- Varith, J., Hyde, G.M., Baritelle, A.L., Fellman, J.K., Sattabongkot, T., 2003. Non-contact bruise detection in apples by thermal imaging. *Innovative Food Sci. Emerging Technol.* 4 (2), 211–218.
- Xing, J., Baerdemaeker, J.D., 2005. Bruise detection on 'Jonagold' apples using hyperspectral imaging. *Postharvest Biol. Technol.* 37, 152–162.
- Xing, J., Bravo, C., Jancsok, P.T., Ramon, H., De Baerdemaeker, J., 2005. Detecting bruises on 'Golden Delicious' apples using hyperspectral imaging with multiple wavebands. *Biosyst. Eng.* 90 (1), 27–36.
- Xing, J., Bravo, C., Moshou, D., Ramon, H., Baerdemaeker, J., 2006. Bruise detection on 'Golden Delicious' apples by vis/NIR spectroscopy. *Comput. Electron. Agric.* 52, 11–20.
- Xing, J., Saeys, W., De Baerdemaeker, J., 2007. Combination of chemometric tools and image processing for bruise detection on apples. *Comput. Electron. Agric.* 56, 1–13.
- Zhang, C., Zhao, C.J., Huang, W.Q., Wang, Q.Y., Liu, S.G., Li, J.B., Guo, Z.M., 2017a. Automatic detection of defective apples using NIR coded structured light and fast lightness correction. *J. Food Eng.* 203, 69–82.
- Zhang, B.H., Dai, D.J., Huang, J.T., Zhou, J., Gui, Q.F., 2017b. Influence of Physical and Biological Variability and Solution Methods in Fruit and Vegetable Quality Non-destructive Inspection by Using Imaging and Near-infrared Spectroscopy Techniques: A Review. <http://dx.doi.org/10.1080/10408398.2017.1300789>.
- Zhao, X.H., Burks, T.F., Qin, J.W., Ritenour, M.A., 2010. Effect of fruit harvest time on citrus canker detection using hyperspectral reflectance imaging. *Sens. Instrum. Food Qual. Saf.* 4, 126–135.
- Zhou, Y., Mao, J.W., Liu, T.B., Zhou, W.J., Chen, Z.W., 2017. Discriminating hidden bruises in loquat by attenuation coefficients estimated from optical coherence tomography images. *Postharvest Biol. Technol.* 130, 1–6.
- Zion, B., Chen, P., McCarthy, M.J., 1995. Detection of bruises in magnetic resonance images of apples. *Comput. Electron. Agric.* 13 (4), 289–299.